

# Nanopatterning of rotating highly oriented pyrolytic graphite (0001) surfaces by ion beam irradiation: Experiments and modeling

Eunsu Lee,<sup>1</sup> J. Seo,<sup>2</sup> J. Muñoz-García<sup>1b</sup>,<sup>3</sup> M. Castro<sup>1b</sup>,<sup>4</sup> R. Cuerno<sup>1b</sup>,<sup>3</sup> and J.-S. Kim<sup>1b</sup>,<sup>2</sup>

<sup>1</sup>*Department of Physics, Sook-Myung Women's University, Seoul 04310, Korea*

<sup>2</sup>*Institute of Advanced Materials and Systems, Sook-Myung Women's University, Seoul, 04310, Korea*

<sup>3</sup>*Departamento de Matemáticas and Grupo Interdisciplinar de Sistemas Complejos (GISC),*

*Universidad Carlos III de Madrid, 28911 Leganés, Spain*

<sup>4</sup>*Instituto de Investigación Tecnológica (IIT) and GISC,*

*Universidad Pontificia Comillas, E-28015 Madrid, Spain*



(Received 17 September 2021; revised 13 January 2022; accepted 20 January 2022; published 16 February 2022)

We produce ordered surface nanostructures on azimuthally rotating HOPG(0001) by irradiation with low-energy ion beams. Thus, small dots at low fluences evolve into cellular structures at large fluences. This transition is a consequence of the fast growth of dots and their subsequent concatenation to form walls along the grain boundaries, leading to cells. The walls compete and ripen with continued ion beam irradiation, resulting in both coarsening and roughening of the cell pattern. We reproduce the same morphological and scaling behavior using different ions, Kr or Ar, so the mechanisms involved in pattern formation and coarsening are robust. We compare the experimental findings with simulations of a nonlinear continuum model based on ion-driven viscous flow, which reproduces many qualitative properties seen in the experiments. Such a comparison underscores the need for a suitable consideration of both external noise and the grain structure of the target to fully account for the large-scale properties of the process.

DOI: [10.1103/PhysRevB.105.085413](https://doi.org/10.1103/PhysRevB.105.085413)

## I. INTRODUCTION

If an energetic ion beam impinges onto a solid substrate, it can cause erosion (sputtering) and displacement of the target material near the surface [1]. After sustained irradiation—tens of minutes for typical ion fluxes of standard broad ion beams, in the order of one ion per nm<sup>2</sup> per second—a nanoscale pattern of either dots or ripples usually forms on the target surface, depending on the sputter geometry. This fact has led to the development of ion-beam irradiation (IBI) as a competitive technique to efficiently nanostructure solid surfaces, as it is a single step, easily scalable, and cost-effective process applicable to virtually any ion/target combination, with target materials ranging from organic to inorganic and from metallic or semiconducting to insulating [2–6]. Considering the stochastic nature of IBI at microscopic scales, the spontaneous formation of patterns by this technique is a highly nontrivial process, and the underlying physics still remains intriguing after four decades of extensive work [2–6].

Classically, the surface structures formed by IBI were seen as a nuisance, as they complicated, e.g., depth profiling by secondary ion mass spectroscopy since their occurrence limits the depth resolution. Zalar [7] proposed easing the problem by rotating the substrate during IBI, since the surface roughness dramatically reduces on the rotating surface, as compared with that on the stationary surface sputtered under otherwise the same sputter conditions. Still, nanoscale surface patterns are widely observed on various substrates rotated during IBI [8–13]. On the rotating surfaces of compound semiconductors such as InP [9,10], GaSb [10], InSb [10], and InAs [10] patterns of nanodot form, exhibiting either hexagonal or square

in-plane symmetry, depending on the incidence polar angle of the ions. For rotating Si surfaces, nanodot patterns show either short-range hexagonal order [12] or chaotic structures [13].

From a theoretical point of view, pattern formation via IBI with surface rotation has been most frequently understood as a particular case of the ion incidence. Let us consider the paradigmatic case of semiconducting targets [2–6] and a static reference situation in which the polar ion incidence angle  $\theta$  is above some threshold value. Then, a periodic ripple structure forms whose wave vector is parallel to the projection of the ion beam on the target plane (parallel ripple pattern). For a target rotating at a sufficiently high speed, nanopatterns are isotropic, with a typical wavelength comparable to that of the ripple structures formed on stationary targets as predicted by well-known continuum models of IBI [14–16]. It is also seen for more microscopic models. For instance, Yasserli and Kree [17] performed kinetic Monte Carlo (kMC) simulations of IBI on rotating substrates, employing Sigmund's theory [1,18] of surface erosion by IBI, and observed growing cellular structures with typical sizes comparable to those of ripples produced on stationary targets. Likewise, Yang *et al.* [19] performed hybrid kMC simulations, employing so-called crater functions obtained from molecular dynamics simulations [4–6], and similarly predicted the formation of dotlike patterns on rotating Si substrates, with typical scales comparable to those of ripples on stationary samples, namely, in the range of tens of nm. It is worth noting that isotropic cellular patterns of much larger sizes in the micron range have been seen and modeled on Si surfaces under isotropic etching conditions by magnetron sputtering [20,21]. In any case, none

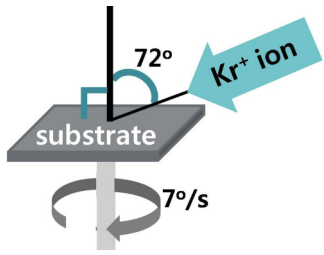


FIG. 1. Schematic of the irradiation geometry with the HOPG(0001) substrate rotating in azimuth. The ion incidence angle equals  $\theta = 72^\circ$  from the surface normal and the angular speed of the rotation is  $7^\circ/\text{s}$  or 1.12 rotations per minute (rpm).

of the theoretical models in these references have yet provided a concrete physical mechanism by which the typical motif (e.g., dots or holes) forming the isotropic pattern is determined on rotating substrates.

Previously, experimental pattern formation by IBI on rotating substrates had been carried out primarily with semiconducting materials. In contrast, in this paper, we consider a semimetal, highly oriented pyrolytic graphite (HOPG) for which a preliminary report has shown formation of cellular patterns on rotating targets undergoing IBI [22]. Here, we study IBI of rotating HOPG(0001) surfaces systematically, which allows us to assess a rather peculiar pattern formation process. Specifically, an isotropic pattern of nanodots evolves into an arrangement of cells at relatively large ion fluencies. The time evolution of the surface morphology features a scaling behavior for various observables like the surface

roughness and pattern wavelength, which we measure. Notably, the typical scales of the cellular structures are roughly a factor of 10 times larger than those of the dots, and seem to be induced by the grain structure of the samples.

In addition, some of the scaling behaviors that we characterize depend on the basic motif which dominates the surface pattern. This contrasts with behavior experimentally assessed, e.g., for Si substrates, for which the pattern dynamics (which unfolds in macroscopic timescales, as in our present case) have been largely independent of the state of order or disorder of the near-surface region of the targets [23]. We compare our experimental observations with predictions of a nonlinear continuum model of surface nanopatterning by IBI, which successfully describes many properties of the process both at early and long irradiation times [24].

The paper is organized as follows. In Sec. II, we provide details on our experiments on IBI of rotating HOPG(0001) substrates. Section III presents our experimental results using  $\text{Kr}^+$  ions. Additional experimental results with  $\text{Ar}^+$  ions are left to an Appendix. Then, we present a continuum model in Sec. IV, which is studied by means of numerical simulations. Section V further discusses the comparison between our experiments and model, providing additional considerations on the scaling behavior found in relation with other experimental and theoretical results in the literature. Finally, Sec. VI summarizes our main results and conclusions.

## II. EXPERIMENTS

IBI is performed in a high vacuum chamber, whose base pressure is maintained at low  $10^{-9}$  Torr. The ion source is of Kauffman type (Physical Electronics, 04-161 Sputter Ion

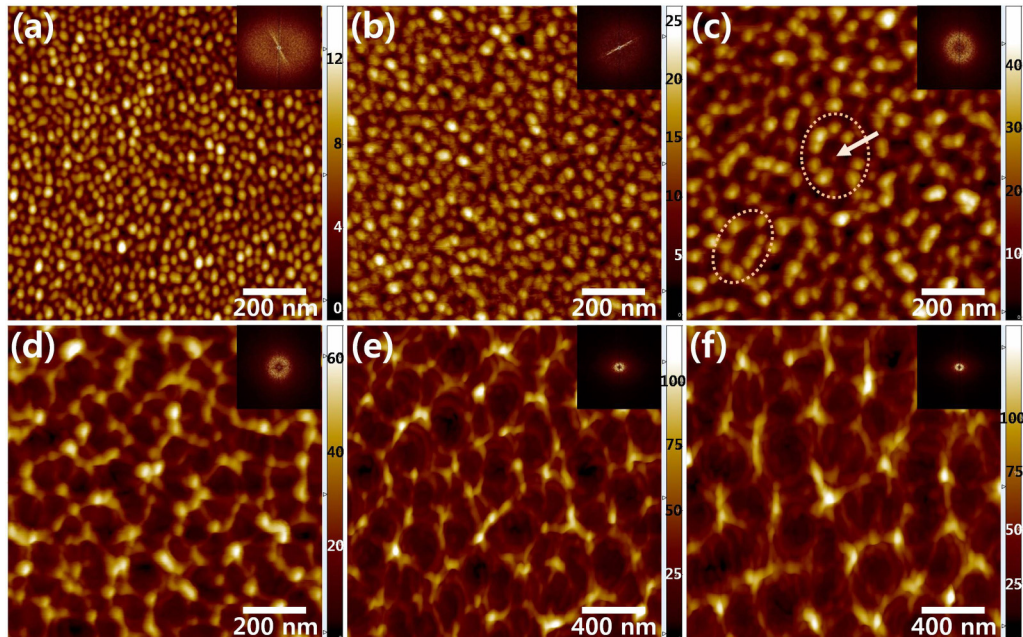


FIG. 2. Irradiation time or fluence dependence of the pattern formed by IBI. The panels show AFM top views of rotated HOPG(0001) surfaces undergoing IBI with  $\text{Kr}^+$  ions for a total irradiation time  $t$  equal to (a) 60 min ( $577 \text{ ion}/\text{nm}^2$ ), (b) 120 min ( $1154 \text{ ion}/\text{nm}^2$ ), (c) 240 min ( $2308 \text{ ion}/\text{nm}^2$ ), (d) 360 min ( $3462 \text{ ion}/\text{nm}^2$ ), (e) 960 min ( $9232 \text{ ion}/\text{nm}^2$ ), and (f) 1440 min ( $13580 \text{ ion}/\text{nm}^2$ ). The inset in each image shows the modulus of the fast Fourier transform (FFT) map of the real-space image in the corresponding main panel. The arrows in (c) indicate some closed loops formed by concatenated dots. The height scales are in nm units.

Gun). The ion beam has a Gaussian intensity profile, the full width at half maximum of which is about 3.5 mm when incident normal to the surface.

In the present paper, we use HOPG(0001) (SPI, ZYA grade) as the substrate. Employing synchrotron-based grazing incidence x-ray diffraction, we found the lateral correlation length of our HOPG to be approximately 350 nm, which was taken as a measure of the mean grain size in our previous work [25]. Since we use the same grade (ZYA grade) of HOPG from the same manufacturer (SPI) in the present experiment as that used in Ref. [25], we also take this as an estimate of the mean grain size of the present HOPG.

The ion species employed are nominally  $\text{Ar}^+$  or  $\text{Kr}^+$ , while ions with higher charges and neutral atoms are not filtered. Unless otherwise specified, the ion energy  $E$  is 2 keV and the target current is around  $10 \mu\text{A}$ , from which the ion flux  $f$  is estimated to be  $0.16 \text{ nm}^{-2}\text{s}^{-1}$ . Since the measured current includes the secondary electron current,  $f$  only sets an upper bound for the actual ion flux. Since  $f$  is fixed throughout the experiments, the ion irradiation time  $t$  and the ion fluence  $F$  ( $= f \times t$ ) will be used interchangeably.

The ion beam impinges onto the rotating substrate at the polar angle  $\theta = 72^\circ$  from the surface normal, see Fig. 1. The angular speed of the rotation is  $7^\circ\text{s}^{-1}$  or 1.12 rotations per minute (rpm). For the rotation of the substrate, we employ an AC servo motor that is controlled by a LabView-based program we have developed.

The surface topography was observed by an atomic force microscope (AFM, Park Systems, XE-100) in the tapping mode. The debris created on the substrates by IBI constantly modifies the AFM tips and distorts the images. Extensive efforts have been devoted to obtaining the image under pristine tip conditions. For image analysis, we utilize both the commercial package SPIP: Image Metrology and homemade software.

### III. RESULTS

In this section, we describe results obtained employing  $\text{Kr}^+$  ions. Results for  $\text{Ar}^+$  ions are fully analogous and are briefly described in the Appendix.

Figure 2 shows the evolution of the patterns formed by sustained IBI of a rotating HOPG(0001) surface with the increase of the ion fluence. Initially, an isotropic dot pattern forms and coarsens with increasing irradiation time. A conspicuous feature is that the basic motif of the pattern changes from a dot in Figs. 2(a) and 2(b) to cellular structure in Figs. 2(e) and 2(f). For intermediate times, the patterns show transitional features in Figs. 2(c) and 2(d).

For stationary HOPG(0001), on the other hand, the motif of the pattern changes from the dot in Figs. 3(a) and 3(b) to the ripple in Figs. 3(c) and 3(d). Most dots are concatenated as indicated by the white arrows in Figs. 3(a) and 3(b) and some evolve into bulged structures as found in the dotted circles in Fig. 3(c), and later into wall-like structures as in the dotted square in Fig. 3(d), leading to a highly disrupted ripple morphology as shown in Figs. 3(c) and 3(d).

Figure 2(a) for  $t = 60 \text{ min}$  ( $F = 577 \text{ ion/nm}^2$ ) shows a pattern of nanoscale dots that do not cover the surface compactly but are well separated from one another. For  $t =$

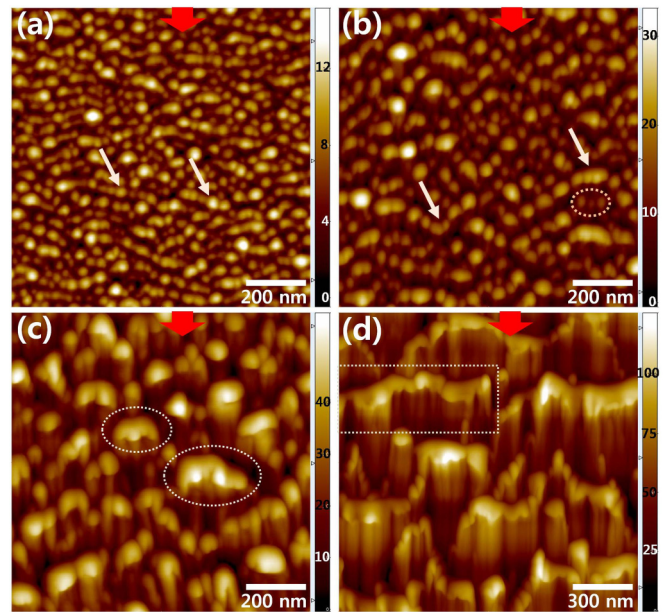


FIG. 3. Pattern evolution on stationary HOPG targets under otherwise the same irradiation condition as employed for the rotating substrates. The panels show AFM top views of stationary HOPG(0001) surfaces undergoing IBI with  $\text{Kr}^+$  ions for a total  $t$  equal to (a) 60 min, (b) 120 min, (c) 240 min, and (d) 960 min. The red downward arrow on top of each image indicates the surface-projected ion beam direction. The white arrows in panels (a) and (b) indicate concatenated dots. The dots enclosed by a dotted ellipse in (b) remain apart from the concatenated dots. Bulged (wall-like) structures are identified with dotted ellipses (rectangles) in panel (c) [(d)]. The height scales are in nm units.

120 min, the pattern is still made of dots as shown in Fig. 2(b). In Fig. 4(a), however, the density of small dots has decreased noticeably, while that of large dots seems unchanged, as observed in a coarsening process whereby large dots grow at the expense of smaller ones [26]. This behavior is common to the rotating and the stationary targets as shown in Figs. 4(a) and 4(b), both also displaying many concatenated dots as observed in Fig. 2(c) and Figs. 3(a) and 3(b), suggesting that common mechanisms operate in the evolution of the patterns on both surfaces.

As  $t$  further increases to 240 min, large dots are well distinguished from small ones and cover most of the surface in Fig. 2(c). The dot density has decreased further, and the distance among bigger dots increases, as suggested by the visual comparison of Figs. 2(a)–2(c) as well as by the dot distribution in Fig. 4. Many of the large dots in Fig. 2(c) appear concatenated to form short curvilinear walls, some forming small closed structures as shown by the dotted circles in Fig. 2(c). In contrast, isolated or weakly connected dots are rarely found, and most of them are distinctively small.

In Fig. 2(d), for the larger  $t = 360 \text{ min}$ , the walls become globally linked to form a cellularlike structure which is not complete, yet rather looks like a network of nanostructures. Some sections are slender and barely linked, while other show a strong modulation in height and width, as a vestige of the concatenated dots.

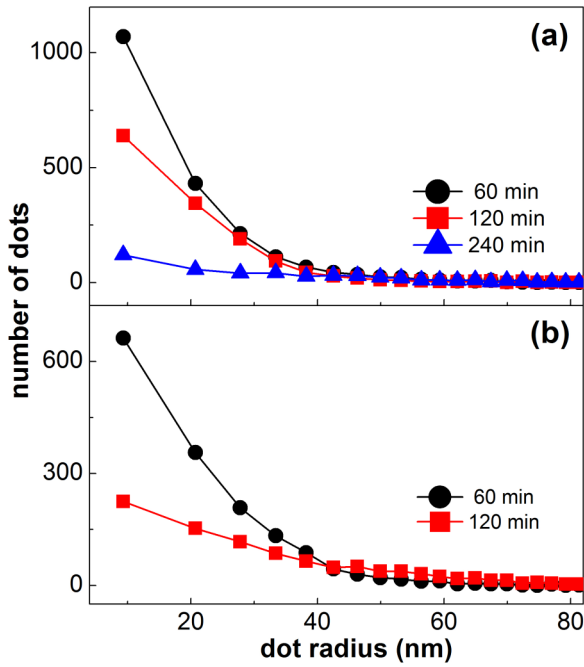


FIG. 4. Irradiation time dependence of the dot-size distribution of the pattern on (a) the rotating surface and (b) the stationary one for IBI using  $\text{Kr}^+$  ions.

For still higher  $t = 960$  min, the cellular pattern has developed with clearly discernible enclosures inside well-defined walls, as seen in Fig. 2(e). The individual dots are no longer identifiable along the walls, while pronounced protrusions are frequent around wall junctions. We will call each enclosure a cell. Their average diameter is at least ten times that of an individual dot, since the cellular structures in Fig. 2(e) evolve from the enclosures that originate from the concatenated dots. [Note the larger scales used in Figs. 2(e) and 2(f) than those in the rest of the panels]. As IBI proceeds further, the cellular structures continue to widen and deepen. This can be appreciated in more detail in Fig. 5(a), which corresponds to a very

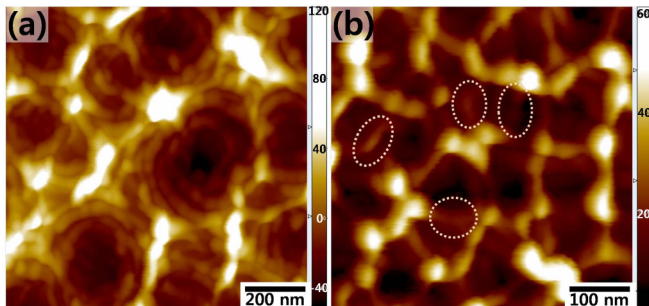


FIG. 5. Detailed structure of cellular structures formed at long  $t$  by  $\text{Kr}^+$  irradiation of rotating targets. (a) Representative AFM top view for  $t = 1440$  min, showing the inner annular configuration of the cellular structures. (b) Similar to panel (a), for an intermediate stage at  $t = 360$  min, showing the competition among growing structures leading to cell coarsening. Structures marked inside the dotted circles will shrink with increasing  $t$ . The height scales are in nm units.

large  $t (= 1440$  min). Indeed, the cellular structures show a multilevel annular structure around their circumference, suggesting that they have grown via the consecutive growth of walls of ever larger radii alongside their previous contour. The space and part of the material for the growth of some cellular structures should be provided by the elimination of the other, in a coarsening process. Indeed, remnants of walls are always observed inside the cells as seen in Fig. 5(b), which are even smaller than the dots that develop for small  $t$ , e.g., in Fig. 2(c), indicating that they have shrunk with increasing  $t$  partly to the benefit of surrounding cell walls.

The cellular pattern may be viewed as a Schwarzite [27,28] or negatively curved sponge carbon truncated by the surface, considering their similar morphologies. Schwarzite is composed of pentagons and heptagons in addition to hexagons of carbon [28]. However, stationary HOPG irradiated by a 2 keV Ar ion beam largely remains crystalline or produces stacked graphene according to Raman spectroscopy [25]. Still, a cellular pattern forms by IBI of rotating targets with 2 keV Ar ions, indicating that it does not originate from Schwarzite, see Fig. 15 in the Appendix. IBI with 2 keV Kr ions should cause more severe damage to HOPG due to the larger momentum transfer from the ions to the surface. When the incident ion energy is increased ( $E > 10$  keV), more serious ion damage develops at the irradiated HOPG, which becomes amorphized [29,30]. Considering this observation, 2 keV Kr IBI may induce some degree of amorphization of HOPG, if any, but it would not transform HOPG into the cellular structure having the atomic structure of Schwarzite.

As indicated by the fast Fourier transformation (FFT) of the surface morphologies provided as insets in Fig. 2, both the dot and the cellular patterns are disordered and isotropic. This fact and the occurrence of a cellular pattern with typical scales much larger than those of individual dots contrast with results on rotating semiconductor substrates [9,10,12,13], which mostly show well-ordered dot patterns.

We quantitatively characterize the dot pattern and the cellular patterns and the transition between them. To this end, Fig. 6 shows the temporal evolution of the surface roughness  $W(t)$ , the areal dot density  $\sigma(t)$ , and the local slope distribution. Here,

$$W^2(t) = \langle (h(\mathbf{r}, t) - \bar{h}(t))^2 \rangle, \quad (1)$$

where  $h(\mathbf{r}, t)$  is the surface height above point  $\mathbf{r} = (x, y)$  on the target plane at  $t$ ,  $\langle \dots \rangle$  represents space average and  $\bar{h}(t)$  is the mean height of an image at  $t$ , and  $\sigma(t)$  is obtained from the cross-sectional area at a height value equal to  $\bar{h}(t)$  as shown in the insets of Fig. 6(b). A characteristic value of the irradiation time  $t_c \approx 345$  min can be identified in the figure, which separates different behaviors. For  $t < t_c$ , the roughness increases as a power law of  $t$  as  $W(t) \sim t^\beta$ , with  $\beta = \beta_1 = 0.94$ , while for  $t > t_c$  the exponent decreases to  $\beta = \beta_2 = 0.47$  so amplitude growth slows down. Note that  $t_c$  is associated with the transition from the dot pattern for  $t < t_c$  to the cellular pattern for  $t > t_c$ , since  $t_c \approx 345$  min nearly corresponds to Fig. 2(d). Generally speaking, the onset of pattern formation is characterized by exponential amplitude growth [31], which, in the presence of large disorder may be observed as power-law increase of  $W$  [21,32,33] with large  $\beta$  values as obtained here for  $t < t_c$ . Meanwhile,  $\beta \approx$

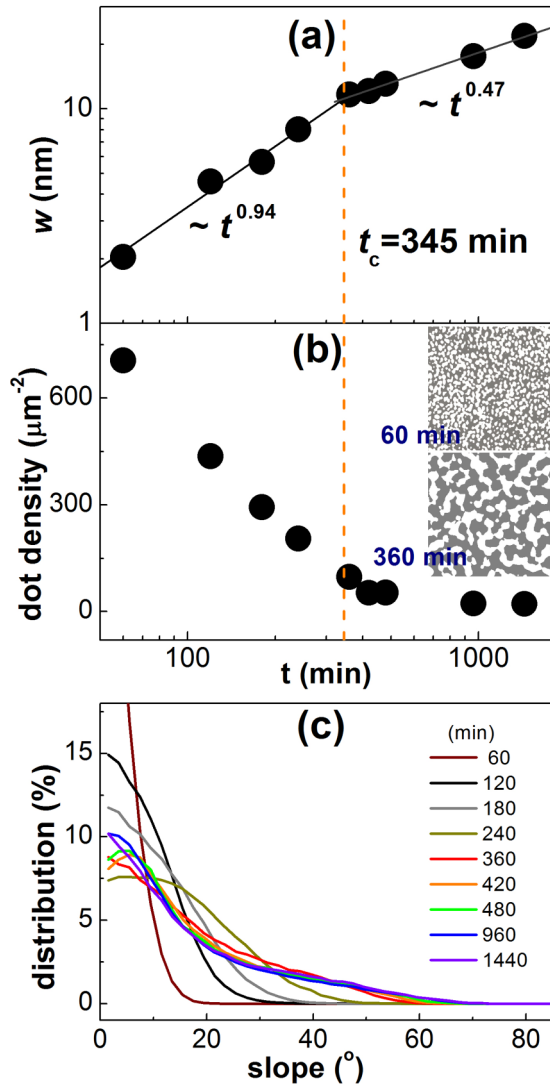


FIG. 6. Irradiation time dependence of (a) the surface roughness  $W(t)$ , (b) the areal dot density  $\sigma(t)$ , and (c) the local slope distribution for  $\text{Kr}^+$  irradiation of rotating targets. The dashed vertical line in (a) and (b) is at  $t = t_c \approx 345$  min. The solid lines in (a) represent power-law behavior as  $W(t) \sim t^\beta$  for the values of  $\beta$  indicated in each case. The insets in (b) show in grey the area covered by dots from the cross-sectional area of AFM snapshots, taken at a height value equal to  $\bar{h}(t)$  for the indicated values of  $t$ .

$1/2$  we observe for  $t > t_c$  is typical of structures which are growing independently of one another [33,34].

The dot areal density  $\sigma(t)$  also shows distinct  $t$  dependencies before and after  $t_c$  in Fig. 6(b). For  $t < t_c$ ,  $\sigma(t)$  drops due both to the demise of the small dots and to the concatenation of the remaining dots as found in Figs. 2(a)–2(c). For  $t$  approaching  $t_c$ , concatenated dots percolate the surface and  $\sigma(t)$  becomes very small. For increasing  $t (> t_c)$ , it continues to decrease, albeit very slowly, due to the coarsening of the cellular structures. Finally, in Fig. 6(c) the distributions of the local slopes along an arbitrary direction, e.g., their horizontal axis, differ notably for  $t < t_c$ , while they become roughly  $t$  independent for  $t > t_c$ , indicating the self-similarity of the

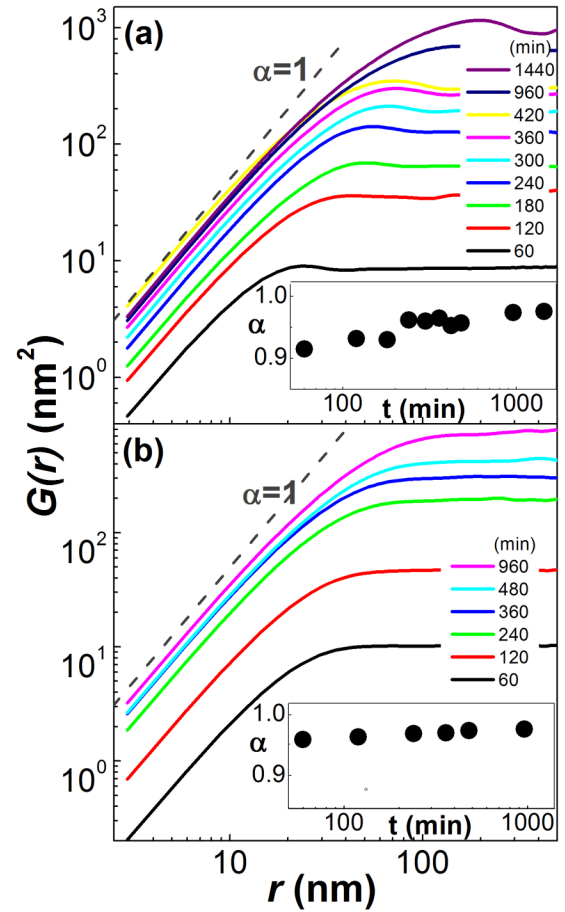


FIG. 7.  $G(r, t)$  as a function of distance and the irradiation time  $t$  shown in the legends for (a) rotating and (b) stationary targets. The units of the legends are minutes of irradiation time  $t$ . Insets show the corresponding value of the roughness exponent  $\alpha$  as a function of  $t$  in minutes.

cellular patterns at  $t > t_c$ , which is not the case for the dot patterns at  $t < t_c$ . See further discussion in Sec. V B.

In addition to the dot areal density, the power-law behavior of the surface roughness frequently correlates with the disorder of the surface morphology [32,33], visually apparent for our dot and cellular patterns. Fluctuations in the values of the surface height can be quantified, e.g., by the height-difference correlation function  $G(r, t)$ , defined as

$$G(r, t) = \langle (h(\mathbf{r}', t) - h(\mathbf{r}' + \mathbf{r}, t))^2 \rangle, \quad (2)$$

where  $r = |\mathbf{r}|$ . Plots of  $G(r, t)$  are shown in Fig. 7 for our full range of  $t$  values, both for rotating and for stationary surfaces. Largely irrespective of incidence conditions and  $t$ , the  $G(r, t)$  functions are seen to increase as a power-law of distance as  $G(r) \sim r^{2\alpha}$  for  $r < \xi(t)$ , where  $\xi(t)$  is a  $t$ -dependent characteristic distance or correlation length, and then saturate to an  $r$ -independent value for  $r > \xi(t)$ . Here,  $\alpha$  is the roughness or wandering exponent [32,33] and in our present case,  $\xi(t)$  coincides with the average dot (cell) size for  $t < t_c$  ( $t > t_c$ ). As seen in Fig. 7,  $\alpha$  is quite close to 1 irrespective of  $t$  or incidence condition. Note also that  $G(r, t)$  curves shift systematically upward with increasing time. For patterns made up by a well-defined motif but which are sufficiently disordered (as

is the case in the present experiments), the scaling behavior just described for the correlation function  $G(r, t)$  has been assessed in many other models and experiments, see, e.g., Refs. [34–38] and therein, and is largely insensitive to the detailed form of the basic motif (say dot or crater) which makes up the disordered pattern [36,37]. From this point of view,  $G(r, t)$  is not an accurate tool to distinguish among different patterns (e.g., dot versus cellular patterns), although the scaling behavior just described is meaningful with respect to the amount of disorder that exists in each time regime and can also guide comparison to theoretical models, as not all of them display this type of behavior.

Overall, Fig. 7 implies that a coarsening process is taking place in which a pattern is dominated by a well-defined characteristic motif (dot or cellular structure) whose typical size  $\xi(t)$  increases with  $t$ . Surface correlations at distances smaller than  $\xi(t)$  are set by the shape of the motif and are weak for larger distances.

To further study how fluence affects the coarsening process, we thus need to quantify the characteristic size of the pattern motif,  $\xi(t)$ , for each value of  $t$ . We will compute this distance from correlation functions in reciprocal space, in particular, from the power spectral density (PSD) [32] well-known to provide more accurate estimates of characteristic scales for disordered surface morphologies [39]. Results are shown in Fig. 8(a), where we consider both rotating and stationary targets. In the former case, as an empirical estimate of  $\xi(t)$ , we obtain the pattern wavelength  $\lambda(t)$  of an AFM image from the peak position of its one-dimensional (1D) PSD [32] along the fast scan direction, say the  $x$  axis. (Here we do not use the radial PSD that seems natural for the isotropic conditions of rotating substrates, since the images are found vulnerable to distortion along the slow scan direction due to the drift of the AFM scanner.) In the case of stationary targets, we need to take into account the in-plane anisotropy of the images like those in Fig. 3. Hence, we consider two different characteristic wavelengths. Since they correspond to the ripple wavelength and the mean uninterrupted ripple length along its ridge or ripple coherence length for ripple patterns like those in Figs. 3(c) and 3(d), we name them, respectively, as  $\lambda_r$  and  $\lambda_c$ ; both are obtained from 1D PSD's of the AFM images along the  $x$  and  $y$  axes, respectively.

Figure 8(a) details the wavelength coarsening process that takes place in each case. For rotating targets, the wavelength indeed increases with time as a power law [26]  $\lambda(t) \sim t^n$  with a coarsening exponent value  $n \simeq 0.59$  which is common to the large and small fluence regimes. Analogously, the coarsening behavior on the stationary surfaces is insensitive to the relative value of the irradiation time with respect to  $t_c$ . As indicated above, in this case we have to distinguish two different characteristic length scales,  $\lambda_r$ , and  $\lambda_c$ . Both wavelengths follow  $t$ -independent power laws with irradiation time  $t$  as  $\lambda_{r,c} \sim t^{n_{r,c}}$  with  $n_r \simeq 0.35$  and  $n_c \simeq 0.62$ .  $\lambda_r$  increases with time at a slower rate than  $\lambda_c$ .

To compare the scaling behaviors found for the rotating and stationary targets, recall from Fig. 3 that the ripples formed in the stationary case are frequently interrupted by bulged structures that adjoin neighboring ripples and severely limit the ripple coherence length  $\lambda_c$ . With increasing  $t$ , such bulged

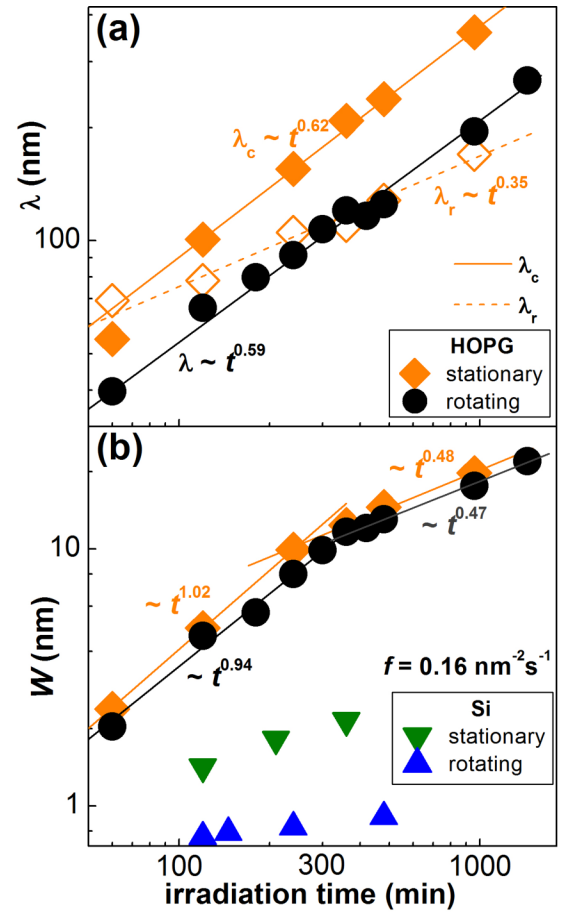


FIG. 8. Scaling behavior with irradiation time  $t$ , equivalently fluence, of (a) the pattern wavelengths  $\lambda(t)$  (for rotating targets) and  $\lambda_{c,r}(t)$  (for stationary targets) and (b) the surface roughness  $W(t)$  of corresponding HOPG substrates irradiated with  $\text{Kr}^+$  ions. For all graphs, straight lines correspond to power laws, as indicated in each case. In panel (a), circles (squares) correspond to rotating (stationary) HOPG substrates. For the stationary case, filled (empty) squares correspond to  $\lambda_c$  ( $\lambda_r$ ). Panel (b) shows additional data obtained on both rotating and stationary Si targets under otherwise the same conditions. For Si, the surface width of the rotating substrate (blue triangle) is notably smaller than that for the stationary one (green triangles), which is in contrast to the case for HOPG.

structures form extended wall-like structures across many ripples in Fig. 3(d), increasing the value of  $\lambda_c$  in such a way that the coarsening exponent of the coherence length  $n_c$  is close to the coarsening exponent  $n$  found on the rotating substrates. We believe that such wall-like structures are relevant to the pattern formation on the rotating surfaces, as discussed below.

In Fig. 8(b), the roughness  $W$  also displays the same crossover behavior for stationary targets as we had already found in Fig. 6(a) for rotating ones. Moreover, the values of the growth exponent  $\beta$  are similar on both sides of  $t_c$  for the rotating and for the stationary HOPG(0001) samples.

The scaling behavior displayed in Fig. 8 shows that the scaling exponents  $n$  and  $\beta$  observed for the rotating targets are similar to those of the stationary HOPG, suggesting that there is possibly a common mechanism controlling the surface dynamics for rotating and stationary targets. Moreover, it is

not  $\lambda_r$ , but  $\lambda_c$ , whose coarsening exponent is similar to that for  $\lambda$  for the rotating HOPG, suggesting that the mechanisms for the formation and growth of the bulged structures on the stationary substrates are relevant to the temporal evolution of the patterns on the rotating substrates.

Having been motivated by the relevance of the behavior of stationary targets to understand the pattern formation seen in the presence of rotation, we need to consider an additional element previously shown to play an important role in the former case, namely, the grain structure of our polycrystalline samples. Indeed, in our previous work with stationary HOPG(0001) targets [25], large dots form preferentially on the illuminated side of grain boundaries since mass displacement should be enhanced there due to the increased exposure to the incident ion beam of the side wall of the stack of weakly bonded graphene layers. Conversely, small dots develop on the terraces of the grains at which mass displacement by the incident ions should occur in relatively small scale due to both the small ion flux on the terrace compared with that at the illuminated side of the grain boundary and the strong carbon-carbon in-plane bonding of the graphene compared with the weak interlayer bonding. The number of large dots is thus largely conserved before their coalescence occurs, as shown in Fig. 4(b), since they grow at the limited locations of the grain boundaries. The population of the small dots decreases as shown in Fig. 4, since ion-irradiation-induced dot ripening can occur via effective mass transport from the small dots on the terrace to the neighboring large dots at the grain boundaries. Continued irradiation of the ion beam concatenates those dots together, forming wall-like structures along the illuminated section of the grain boundary, as shown in Fig. 3(c). They are separated by distances similar to the mean size of the grain boundary. Further IBI also induces ripening, but now among neighboring wall-like structures, leading to coarsening of the wall pattern as noticed by comparing Fig. 3(d) with Fig. 3(c). This coarsening behavior via the ripening process indicates that mass transport among the walls are efficient during IBI. (See also Fig. 5 in Ref. [25] and the related discussion therein.)

When the substrate is rotated during IBI, the walls can form in all directions around the grain boundaries and the cellular structures develop at the grain sites. Indeed, concatenated dots tend to form closed loops as shown in Fig. 2(c). Once the walls become globally interlinked with the increase of  $t$ , a cellular pattern forms, as observed in Figs. 2(e) and 2(f). The change of the basic pattern motif on the rotating surfaces from the dot to cellular structure in Fig. 2 is thus traced back to the change of the motif from dot to wall-like structure on stationary surfaces in Fig. 3.

The cellular pattern coarsens with a coarsening exponent  $n$  approximately equal to  $n_c$  on stationary surfaces as shown in Fig. 8(a) and its coarsening mechanism is also traced back to that case. As discussed above, on the stationary surface the dots at the grain boundary grow during IBI at the expense of those at the terrace and form wall-like structures. During continued IBI, ripening occurs among the walls. Both processes make  $\lambda_c$  longer as noted in Figs. 3 and 8(a). This observation provides a hint on the coarsening mechanism of the cellular structure forming on rotating HOPG. Now, large dots grow around the grain boundary during IBI to

form the closed loops of concatenated dots in Fig. 2(c) and further grow to the walls at the expense of dots on the terrace. As IBI continues, some walls grow further, while the others dwindle as found in Fig. 5(b), as also observed on stationary surfaces. The enlarged walls interconnect to form ever-wider cells, repeatedly, some showing well-defined concentric wall structures as seen in Fig. 5(a). That behavior can be viewed as an isotropic analog of the growth of the wall pattern on stationary surfaces, explaining why the scaling exponents  $\beta$  and  $n_c$  for  $\lambda_c$  on the stationary HOPG take the same values as  $\beta$  and  $n$  for the rotating surfaces.

#### IV. CONTINUUM MODEL

Predictive modeling of surface nanostructuring by IBI remains a challenging task which to date has not been fully accomplished [4–6], as it requires describing processes that span several orders of magnitude in time (from tens of picoseconds for relaxation of collision cascades to minutes for steady-state surface morphologies) and space (from nm for the extent of collision cascades to a micron for, e.g., our present cellular patterns). Nevertheless, it is worth trying to rationalize the findings described in previous sections in terms of current models of the process, allowing us to appreciate the novelties brought about by the present experiments and identify future lines of progress in the theoretical understanding of the results in the previous sections.

We consider continuum modeling best suited to reach the macroscopic times reached in our experiments. For example, entering the cellular-pattern regime requires around  $10^3$  minutes of irradiation time. Moreover, significant descriptions require allowing for nonlinear effects: Classic continuum models that describe the onset of pattern formation by IBI [40,41] provide evolution equations for the local target height velocity, which is assumed proportional (linear) to perturbations of the height for a uniform flat morphology. While such an approximation can already describe many nontrivial experimental properties like, e.g., incidence angle conditions for pattern formation, it cannot account for others, like wavelength coarsening, known to be associated with nonlinear effects [42,43]. Then, among the various nonlinear models available in literature, most of them—e.g., those related with the so-called Kuramoto-Sivashinsky (KS) equation [44] and its diverse variants, see, e.g., in Refs. [4–6] for a partial account—describe patterns characterized by a single length scale, as the basic motif (dot or ripple undulation) repeats itself periodically in a close-compact fashion. In contrast, the rotation experiments discussed in the previous section speak of well-separated surface structures.

We recently introduced a nonlinear continuum model that successfully accounts for many experimental properties of IBI for the paradigmatic case of Si targets that, like many others, are or become amorphous under irradiation by noble gas ions at the present low-to-medium energy range [24]. The main assumption of the model is that the damage caused by the ion irradiation in a near-surface region of small thickness,  $h_0$ , is relaxed via (ion-induced) viscous flow. This physical picture was already employed in Ref. [25] to rationalize experiments on stationary HOPG targets. As a result of this hydrodynamic response of the target, strong nonlinearities emerge from the

balance between destabilizing and relaxational mechanisms. Specifically, for a stationary target undergoing IBI at an oblique incidence angle  $\theta$ , the evolution equation for the target thickness  $h(\mathbf{r}, t)$  reads [24]

$$h_t = -a_1 h h_x - a_2 h^2 h_x + \nabla \cdot (h^2 \mathbf{B} \cdot \nabla h) + c \nabla \cdot (h^3 \nabla h) - \gamma \nabla \cdot (h^3 \nabla \nabla^2 h), \quad (3)$$

where the coefficients of the various terms are

$$a_1 = \frac{3G_s \sin(2\theta)}{2\mu}, \quad a_2 = \frac{2G_b \sin(\theta)}{\mu}, \quad \gamma = \frac{\sigma}{3\mu}$$

$$\mathbf{B} = \begin{bmatrix} \frac{3G_s \cos(2\theta)}{2\mu} & 0 \\ 0 & \frac{3G_s \cos^2(\theta)}{2\mu} \end{bmatrix}, \quad c = \frac{2G_b \cos(\theta)}{3\mu}. \quad (4)$$

Here,  $G_s$  and  $G_b$  are parameters characterizing the residual stress distribution induced by irradiation in terms of its value at the free surface and its gradient across the bulk of the damaged layer, respectively;  $\mu$  is ion-induced viscosity, and  $\sigma$  is surface tension. As discussed in Ref. [24], the continuum model leading to Eq. (3) primarily addresses incidence conditions close to the critical angle for pattern formation, where mechanisms, like sputtering—which break mass conservation—seem to play a secondary role. We expect this model to still be meaningful for our present experiments, as non-mass-conserving sputtering-induced nonlinearities have been shown to efficiently arrest coarsening behavior [16,45]. Moreover, note that the derivation of Eq. (3) in Ref. [24] assumes that the amorphized layer has already formed and reached a steady-state characterized by an average depth  $h_0$ , whose value is of the order of the ion penetration depth. Small perturbations around this value at different positions will provide the initial condition with which the equation is to be integrated. Moreover, the interface between the irradiated and unirradiated ( $i-u$ ) target is assumed to remain flat at  $h=0$ . A more comprehensive model of the process would also include the time regime in which the amorphized layer evolves from the pristine unirradiated condition into such a steady state, allowing for a nonplanar  $i-u$  interface [46]. At the present state of development of the theory, this remains a challenge for future work.

Equation (3) is highly nonlinear and happens to bear an intimate relation to continuum models of interfacial dynamics of thin and ultrathin liquid films [47,48], a topic we will address later below. In particular, in that context the local interface velocity is known to depend on the local value of the thickness (or depth) of the layer which is flowing, hence the right-hand side of Eq. (3) not only depends on derivatives of  $h$ , but also on the value of  $h$  itself. Although this contrasts with many other continuum models of IBI [4], it possibly correlates with their different ranges of validity in terms of experimental conditions. Further, detailed relations can be established between terms appearing in Eq. (3) and well-known models of thin fluid films [47,48], e.g., the term with coefficient  $\gamma$  in Eq. (3) plays the same role as in that context [47,48], namely, relaxation of surface features by surface tension. Concerning the remaining terms in the equation, those with coefficients  $a_{1,2}$  are convective nonlinearities implementing the external driving by the ion beam, similar to those with coefficients  $\mathbf{B}$  and  $c$ . The difference is that the latter two contribute to the

onset of pattern formation at linear order, which is not the case for the former two [24].

The parameters in Eq. (3) depend on the experimental conditions as detailed in Eqs. (4). The ion incidence angle is already explicit, while additional system specifics like the ion/target combination and the ion energy determine  $h_0$ ,  $G_s$ ,  $G_b$ ,  $\mu$ , and  $\sigma$ . Large uncertainties affect the accurate values of these constants, but in some cases, like  $\text{Ar}^+$  of Si targets, some orders of magnitude estimates are available in the literature, see Ref. [24]. On the other hand, as shown in that reference, the morphological behavior predicted by Eq. (3) depends on two *independent* parameters only: the incidence angle  $\theta$  and the dimensionless ratio  $g = G_b h_0 / G_s$ .

The main qualitative conclusion is that generically a nonzero threshold incidence value  $\theta_c$  exists such that a ripple pattern forms for  $\theta > \theta_c$ , while irradiated surfaces remain featureless if  $\theta < \theta_c$ ; see Ref. [24] for additional properties. As noted above, such a condition for pattern formation stems from the properties of Eq. (3) under a linear approximation. Among its nonlinear properties, an important one for our present context is that this continuum model can describe patterns whose features are well separated and not necessarily closely packed together. Explicit examples of such ripple formation on stationary targets for  $\theta > \theta_c$  have been provided via numerical simulations [24].

In our present case, we wish to describe experiments on a rotating target on the basis of Eq. (3). Following previous similar modeling approaches to Zalar rotation [15,16], we perform a rotation of angle  $\varphi$  in the target coordinates to a new primed coordinates system, as

$$x' = x \cos \varphi + y \sin \varphi, \\ y' = -x \sin \varphi + y \cos \varphi. \quad (5)$$

By performing this change of variables in Eq. (3), we obtain an equation (not shown) for a system in which the projection of the ion beam on the target plane is at angle  $\varphi$  with the  $x$  axis. Next we assume that the target is rotating at a constant speed which is much higher than the arrival rate of ions, so, effectively, it is as if irradiation were taking place under all possible azimuthal incidences simultaneously. The effective evolution equation is then obtained by averaging over all values of the rotation angle,  $\varphi \in [0, 2\pi]$ , resulting in

$$h_t = \bar{b} \nabla \cdot (h^2 \nabla h) + c \nabla \cdot (h^3 \nabla h) - \gamma \nabla \cdot (h^3 \nabla \nabla^2 h), \quad (6)$$

where  $\bar{b} = 3G_s[1 + 3 \cos(2\theta)]/(8\mu)$ . Equation (6) is our continuum model for the rotating targets. Note it is simpler than the original Eq. (3), as the convective terms which break the  $x \leftrightarrow -x$  cancel out after angular average. Still, the parameters entering Eq. (6) depend nontrivially on those characterizing the ion-induced viscous relaxation dynamics, in particular, on the incidence angle  $\theta$ . For later discussion, it is interesting to further approximate Eq. (6) to write a (so-called weakly nonlinear [47,48]) equation for small deviations  $\tilde{h}(\mathbf{r}, t)$  of  $h(\mathbf{r}, t)$  around the uniform solution  $h_0$ . The result reads

$$\tilde{h}_t = \underbrace{v_r \nabla^2 \tilde{h} - \mathcal{K}_r \nabla^4 \tilde{h}}_{\text{Linear terms}} + \underbrace{\Lambda_r \nabla \cdot (\tilde{h} \nabla \tilde{h}) - \mathcal{K}'_r \nabla \cdot (\tilde{h} \nabla \nabla^2 \tilde{h})}_{\text{Non-linear viscous flow+ surface tension}}, \quad (7)$$

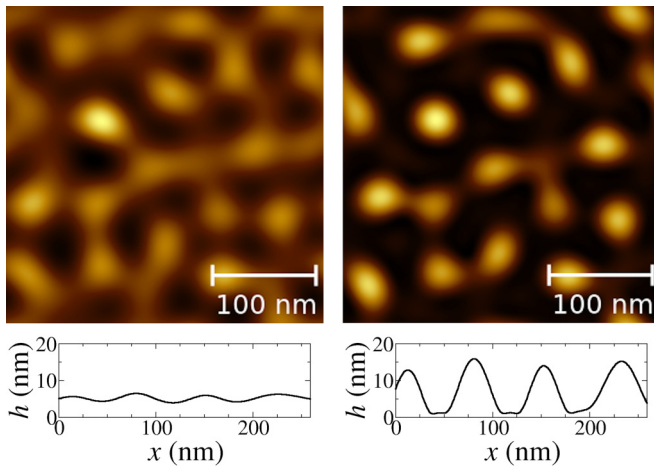


FIG. 9. Surface morphologies from numerical simulations of the full strongly nonlinear Eq. (6) for 2D targets at  $t = 89$  min ( $t = 154$  min) on the left (right) panel, using the parameters indicated in the text. The plot below each image shows a representative 1D cut.

where  $\nu_r = h_0^2 \bar{b} + ch_0^3$ ,  $\Lambda_r = 2h_0 \bar{b} + 3ch_0^2$ ,  $\mathcal{K}_r = \gamma h_0^3$ , and  $\mathcal{K}'_r = 3\gamma h_0^2$ . This equation is a variant of the KS equation [4–6], which differs from it by the conserved nonlinearity with parameter  $\Lambda_r$  and the additional nonlinear surface-tension term with coefficient  $\mathcal{K}'_r$ . Building upon well-established knowledge in IBI modeling [4–6], for instance, now it is much more transparent that an isotropic dot pattern will form provided  $\nu_r < 0$ , which ultimately depends on experimental conditions.

To explore the surface dynamics predicted by the full Eq. (6), we resort to numerical simulations, as the model is still highly nonlinear. We employ the same finite-difference scheme as in Ref. [24], with lattice parameter  $\Delta x = 1$  nm and time step  $\Delta t = 10^{-5}$  min, and checking that mass is conserved, as the continuous equation expresses mathematically a conservation law [24]. We use periodic boundary conditions on the target plane and an initial thickness  $h(x, y, 0) = h_0$ , perturbed by zero-mean, Gaussian white noise with 0.1 nm standard deviation.

As mentioned above, detailed knowledge of the precise numerical values that the original parameters  $G_s$ ,  $G_b$ ,  $\mu$ , etc. take in a precise experiment is unfortunately lacking in most cases. To be specific, we will choose a parameter condition justified in Ref. [24] to be reasonable in orders of magnitude for 1 keV  $\text{Ar}^+$  of Si, while leading to surfaces with a high degree of disorder, akin to our present experiments on HOPG. Specifically, we set  $\theta = 70^\circ$ ,  $G_s = 0.4$  GPa,  $G_b = -0.1$  GPa  $\text{nm}^{-1}$ ,  $\sigma = 10$  GPa nm,  $\mu = 0.83$  GPa min, and  $h_0 = 5$  nm, implying  $\bar{b} = -0.23$   $\text{min}^{-1}$ ,  $c = -0.027$   $\text{nm}^{-1}$   $\text{min}^{-1}$ , and  $\gamma = 4$   $\text{nm min}^{-1}$ .

Figure 9 displays representative surface morphologies at two different times, together with 1D cuts of the corresponding 2D topographies. The left panel shows a relatively incipient isotropic dot pattern, for which the dots have relatively sinusoidal shapes (as expected at early times when linear terms dominate in the equation). Note that the interdot separation improves with increasing  $t$  (or  $F$ ). The formation mechanism is perhaps most simply rationalized via the

approximate equation, Eq. (7): As  $\nu_r < 0$ , the linear terms predict the formation of a periodic pattern of dots with size  $\ell \simeq [\mathcal{K}_r / (-\nu_r)]^{1/2}$ , just as in the KS equation [4].

With increasing time, the dots lose their previous up-down symmetric shape and the thickness of the damaged layer in-between them shrinks, as in fluid dewetting experiments [48], while the 2D arrangement of dots is not very well-ordered, again similar to fluid dewetting. Within this analogy, fluid retreats from interdot regions and accumulates in some dots at the expense of others, leading to dot coarsening. Again, in terms of Eq. (7), the nonlinear porous-medium-like nonlinearity [47,48] with coefficient  $\Lambda_r$  controls the in-plane coarsening of the individual dots, with the nonlinear surface tension term with coefficient  $\mathcal{K}'_r$  smoothing out surface features during this regime.

The analogy with fluid dewetting is further strengthened by studying the time evolution of the dot density in the simulated morphologies. Results are provided in Fig. 10, where the dot density is plotted as a function of time and the corresponding surface morphologies are shown. For this, we also plot the dot density as obtained at  $\bar{h}(t)$ , as was done for the experimental morphologies in Fig. 6(b). The dot density is seen to decrease monotonically with increasing irradiation time, and at rates similar to those in the experimental results.

Further, we can assess the space correlations of these simulated surface morphologies via the height-difference correlation function,  $G(r, t)$ , shown in Fig. 11. Although the number of individual dots in each image is smaller than in the experimental case (recall Fig. 7), the behavior of  $G(r, t)$  is quite similar, with a short-scale scaling behavior as  $G \sim r^{2\alpha}$  with  $\alpha \simeq 0.94$  which saturates at distances similar to the dot size. The existence of oscillations at sufficiently high  $r$  is related to the lack of noise in the simulated morphologies (in contrast with the experimental ones), a topic to which we will come back later below.

Producing morphologies like those in Fig. 9 is computationally quite costly. At this, we can exploit the isotropy of the pattern and try to gain some more quantitative understanding of the process by performing simulations for 1D substrates, in which we neglect the dependence of  $h(x, y, t)$ , e.g., on the  $y$  coordinate. We thus consider the particular case of Eq. (6) for 1D targets, which reads

$$h_t = \bar{B} \partial_x (h^2 \partial_x h) + c \partial_x (h^3 \partial_x h) - \gamma \partial_x (h^3 \partial_x^3 h). \quad (8)$$

From now on, we consider numerical simulations of Eq. (8) using the same parameter values as in Fig. 9. Figure 12 shows representative surface morphologies for total irradiation times which are even longer than those in Fig. 9. The coarsening process of the dot structures can be seen in more detail, as the evolution of single dots can now be traced during the irradiation process (note the large difference in scales between the horizontal and vertical axes in Fig. 12): indeed, the damaged layer separating single dot structures retreats and that material leads to growth of the individual dots, which compete among each other in this process. There is a wide distribution of interdot distances, which do not necessarily coincide with the individual dot sizes.

The evolution of the dot pattern can be examined more quantitatively. Thus, the top panel of Fig. 13 shows the surface roughness obtained from numerical simulations of the

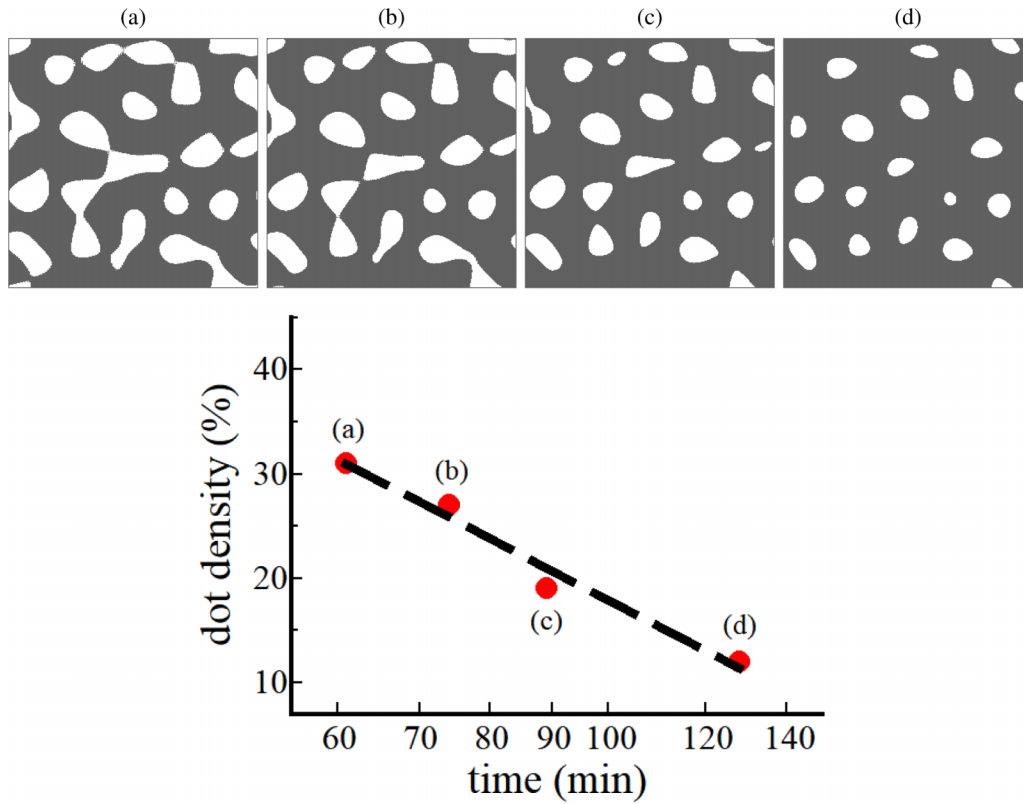


FIG. 10. Log-linear plot of the areal dot density versus irradiation time from numerical simulations of the full strongly nonlinear Eq. (6). As in Fig. 6, the area covered by dots (shown here in white, in the corresponding boxes on the upper row) is obtained from the cross-sectional area of 2D surface morphologies, taken at a height value equal to  $\bar{h}(t)$  for the corresponding value of  $t$ . The physical size of the gray-white boxes is the same as for the 2D snapshots in Fig. 9.

1D strongly nonlinear Eq. (8). The bottom panel of this figure shows the time evolution of the distance,  $L$ , from the origin to first maximum of the height-height correlation function

$$C(x, t) = \langle h(x', t)h(x' + x, t) \rangle, \quad (9)$$

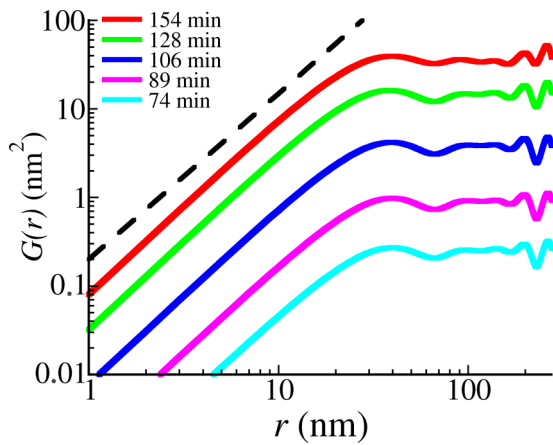


FIG. 11. Height-difference correlation function  $G(r, t)$  as obtained from numerical simulations of Eq. (6) for different simulation times (including the two surface morphologies shown in Fig. 9). As a visual reference, the straight dashed line corresponds to power-law behavior as  $G(r) \sim r^{1.87}$ .

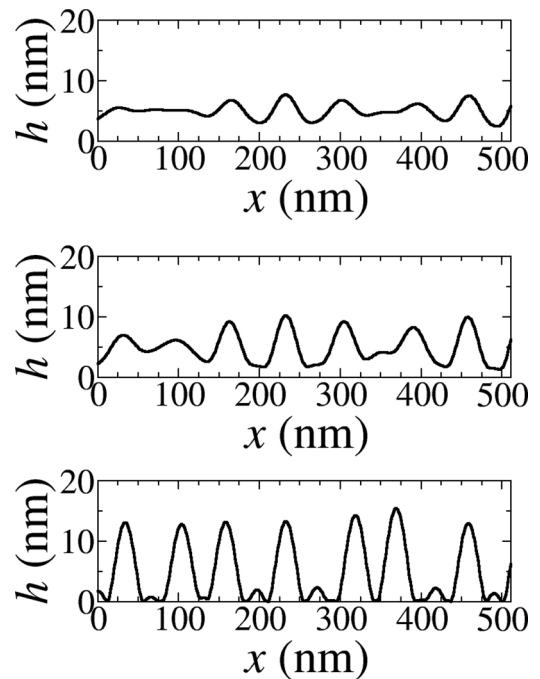


FIG. 12. Surface morphologies from numerical simulations of the strongly nonlinear Eq. (8) for 1D targets at  $t = 154, 184,$  and  $552$  min top to bottom, using the parameters given in the text.

which provides an estimate of the average dot size and of  $\xi(t)$  in our present case, and more suited to the limited statistics of our numerical simulations [32]. For times  $t \lesssim 200$  min, the surface roughness displays very fast growth, which changes into logarithmic behavior  $W \sim \ln t$  at the longest times. However, the coarsening behavior of the dot pattern does not seem to be very sensitive to the growth rate of the roughness, past the very early linear regime. Although the accuracy of our measurements is conditioned by the limited statistics and by the steplike behavior of  $L$ , the overall trend of the dot size is not unlike the  $t^{1/2}$  power law roughly seen in the experiments of Sec. III, and faster than predicted by previous continuum models for IBI of rotating targets [16].

## V. DISCUSSION

Surface nanostructuring of HOPG via IBI of rotating targets is peculiar as compared to the analogous process on other materials, such as Si. This is seen in Fig. 8(b), where the seminal idea of Zalar rotation is seen to work better in the latter than in the former. Indeed, Zalar rotation decreases the roughness of Si targets as compared with stationary samples, but this is not the case for HOPG, rotating, and stationary targets featuring very similar values of the roughness. In spite of this fact and of HOPG being a semimetal, we have seen in the previous section that a model developed for targets which become amorphous under IBI allows us to rationalize the properties of the nanodot pattern experimentally assessed in Sec. III. This can relate to the applicability of Eq. (3) down to very small values of the thickness  $h_0$  of the damaged layer [4,6], in whose limit the related hydrodynamic model well reproduces results from kinetic-type models more naturally applied to metallic systems [4,6]. A classic example of this was provided by Orchard [49], who showed that the mathematical description of viscous flow, once confined to a sufficiently thin surface layer, coincides with that of thermal surface diffusion [50,51].

In this section, we provide some further discussion on the comparison of the experiments reported in Sec. III with the continuum model discussed in Sec. IV and with additional results from literature and elsewhere, some of them briefly indicated in the previous sections.

### A. Continuum model

Returning to the comparison of our simulations with the experimental results, note that, for the sake of definiteness, we have employed parameter values in our simulations that provide reasonable order-of-magnitude estimates as based on IBI of Si targets [24]. However, quantitative differences between this parameter set and a more accurate one for HOPG targets may account for some of the discrepancies between our experimental observations and simulation results. Moreover, the highly nonlinear Eq. (3) is an approximation from a full viscous flow model in which terms are dropped, and this may hinder some quantitative comparison to experimental data.

In addition to the above, two important aspects stand out with respect to the comparison between experiments and model: (i) Our present simulations seem to reproduce the dot pattern adequately but cannot produce cellular patterns and

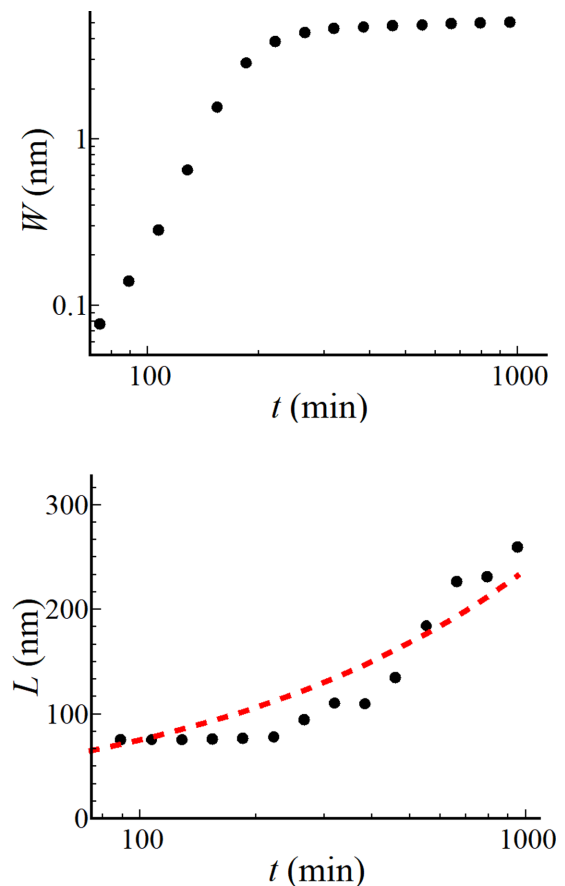


FIG. 13. Surface roughness (top panel) and first maximum of the height-height correlation function as functions of irradiation time, from numerical simulations of the full strongly nonlinear Eq. (6) for 1D targets, using the parameters indicated in the text. As a visual reference, the red dashed line in the bottom panel represents power-law behavior as  $L \propto t^{1/2}$ .

(ii) some of the experimental scaling exponent values are not correctly reproduced.

(i) As discussed at length in the previous section, we believe that a determining factor for the formation of the cellular pattern is the grain structure of the samples, which is nowhere implemented in our continuum model. We are aware that the initial correlations in the surface morphology can quite strongly influence the surface behavior reproduced by continuum models [45,52–54] in spite of the fact that the properties of the residual stress distribution induced by the ion beam are largely independent of the specific state of order of the initial near-surface layer of the target [55]. Hence, we acknowledge the need to incorporate the grain structure into future simulations. Note, this task is a computational challenge, as it requires reaching very large system sizes to assess the collective behavior of cellular structures, which is seen at a distance a tenfold factor larger than that required to assess the statistics of dots, barely reached at, e.g., in Fig. 9.

(ii) The experimental values for the growth exponent  $\beta$  are not accurately reproduced by our simulations: while our continuum model predicts exponential and logarithmic ( $\beta \approx 0$ ) behavior for the roughness at short and long irradiation times, respectively, experiments indicate  $\beta_1 \simeq 1$  and  $\beta_2 \simeq 1/2$  in the

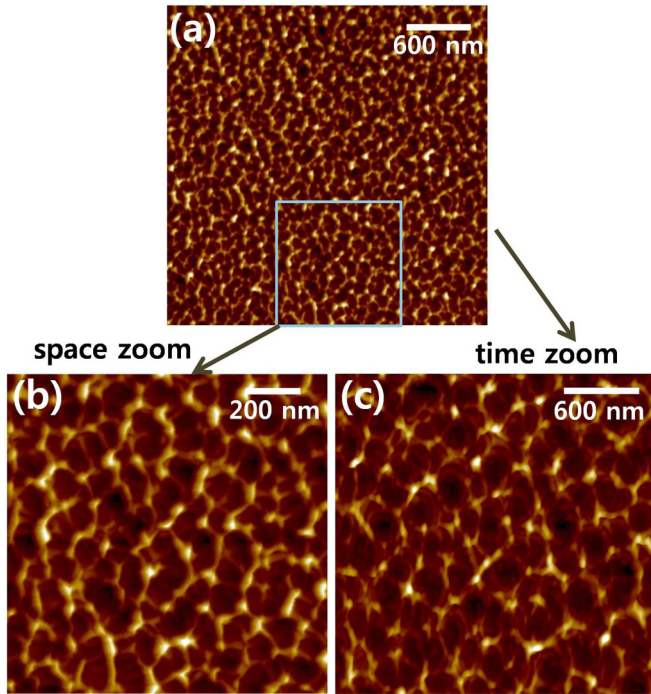


FIG. 14. Space-time self-similarity of the cellular pattern formed by  $\text{Kr}^+$  IBI of rotating targets for  $t > t_c$ . (a) AFM image of the pattern for  $t = 420$  min ( $4039$  ion/ $\text{nm}^2$ ) and (b) zoomed-out image of the marked square area in panel (a). (c) AFM image of the surface for  $t = 960$  min ( $9232$  ion/ $\text{nm}^2$ ). The images in (b) and (c) are statistically equivalent.

corresponding  $t$  or fluence regimes. As noted in the previous paragraph, our simulations do not reach the cellular regime due to the lack of implementation of a grain structure for the target. In any case, we expect the long-time exponent of the roughness to be strongly affected by the incorporation of noise. For example, uncorrelated growing structures are known to feature  $\beta \simeq 1/2$  in the presence of stochastic fluctuations [36,37] and this might account for the large-fluence behavior. With respect to the small-fluence regime, note again that the continuum model discussed in this section is deterministic. Stochastic noise is known to be quantitatively relevant to IBI modeling [44,56], while it is also reported to modify (deterministic) exponential growth of the roughness into power-law behavior with very large exponents  $\beta \approx 1$  [21,32].

In connection with these considerations, we expect that the addition of noise to our continuum model may lead to quantitative predictions which are closer to the experimental results. This is also expected to come at a high computational price. A relevant example is provided by studies on (nano)pattern formation by fluid dewetting [47,48]. As noted above, Eqs. (3), (6), and (8) are closely related with similar models studied in such context [47,48]. There, recent work has shown that thermal noise realistically accelerates the timescales of droplet formation and leads to droplet distributions which are closer to those experimentally observed than those predicted by deterministic models [57,58]. Interestingly, noise also guarantees an approach to an asymptotic equilibrium state via uninterrupted droplet coarsening with characteristic

exponents whose value may be influenced by the fluctuations. However, reproducing these interesting quantitative properties does come at a high computational cost, which has thus far limited simulations to 1D systems [58,59].

### B. Further considerations on scaling behavior

The dot and the cellular patterns identified in Sec. III both exhibit different types of scaling behavior. Frequently scaling is a reflection of some degree of universal behavior [26], hence we may try to identify similar scaling modes in other interface contexts which may aid further understanding of our present results.

Actually, scaling behavior had been previously found for IBI of stationary HOPG targets at somewhat higher energies, using 5 keV  $\text{Xe}^+$  ions at oblique incidence [60]. Highly disordered ripple morphologies were found, which resemble those of Ref. [25], especially for higher incidence angles. Moreover, substantial coarsening of the ripple structures was observed with increasing fluence. No information was provided on coarsening exponent values, while the roughness exponent found at the largest fluences was relatively low,  $\alpha \approx 0.35$ . These ripple structures were addressed in more detail in Refs. [61,62], employing both, 2-50 keV  $\text{Ar}^+$  and  $\text{Xe}^+$  ions, although these works addressed on the energy and temperature dependencies of the ripple wavelength. Albeit at somewhat higher energies, overall these results also obtain disordered ripple patterns on stationary HOPG substrates, with strong coarsening behavior.

In the case of rotating patterns, we distinguish dot patterns at relatively small fluences followed by cellular structures at larger fluences. We next discuss additional results in the literature regarding similar structures.

#### 1. Dot pattern

For  $t < t_c$ , when the dot pattern forms, the coarsening exponent and the growth exponent are  $n \simeq 0.59$  and  $\beta \simeq 0.94$  from Figs. 8(a) and 8(b), respectively. In addition, the roughness exponent is  $\alpha \approx 1$  from the height-difference correlation function in Fig. 7. These surface morphologies demonstrate a sort of mixed topography in which individual structures which are growing fast in amplitude and size (coarsening) arrange themselves into a pattern which displays a large degree of disorder.

*Cauliflower structures.* Quite similar exponents values,  $\alpha = \beta = 1$ , have also been observed for cauliflowerlike surface structures found across many length scales, including cauliflower plants, combustion fronts, and thin solid films grown by chemical vapor deposition [21]. These are instances of extremely disordered patterns in which the growth of a correlation length on the surface with dynamic exponent  $z = 1$  is perceived as a coarsening process of the surface structures, the equality  $\beta = \alpha/z$  being fulfilled as a manifestation of so-called surface kinetic roughening behavior [32,33]. The corresponding surface dynamics has been described quantitatively by a stochastic continuum model [21]. Although this model does predict the formation of cellular structures, it does not reproduce the change of the basic pattern motif between dots and cells which is observed in our experiments.

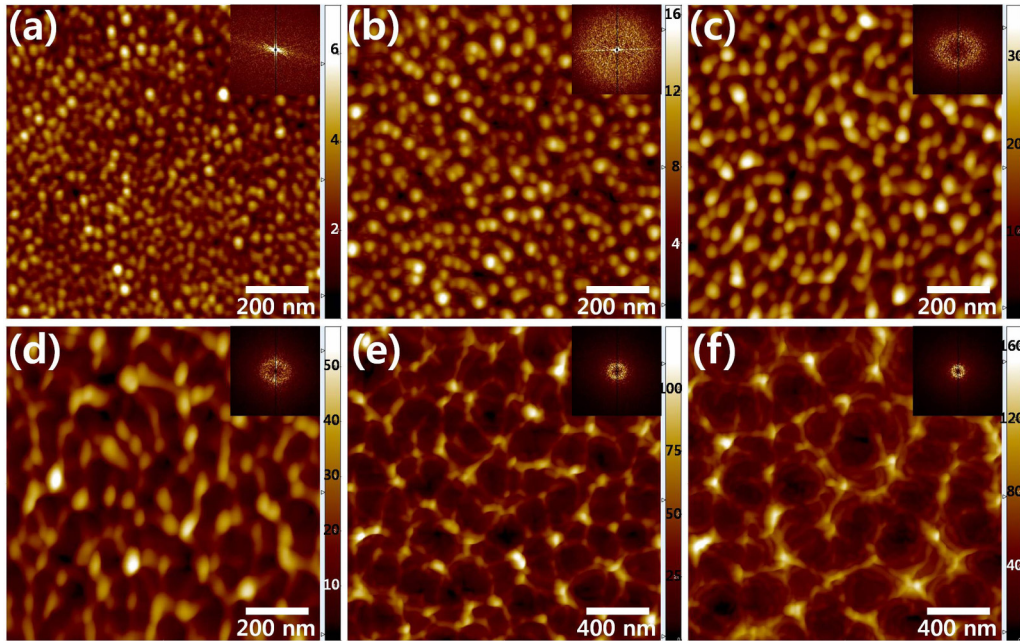


FIG. 15. Fluence dependence of the pattern formed by IBI. The panels show AFM top views of rotated HOPG(0001) surfaces undergoing IBI with  $\text{Ar}^+$  ions for a total irradiation time  $t$  equal to (a) 60 min, (b) 120 min, (c) 360 min, (d) 480 min, (e) 960 min, and (f) 1440 min. The inset in each image shows the modulus of the fast Fourier transform (FFT) map of the real-space image in the corresponding main panel. The height scales are in nm units.

*Shadowing effects.* A different continuum model [63] that takes into account shadowing effects during thin film deposition predicts  $\beta = 1$  and  $1/z = 0.66$ , which are similar to our  $\beta \simeq 0.94$  and  $1/z \sim n \simeq 0.59$  before  $t_c$ . Indeed, approaching  $t_c$ , most of the dots have local slopes that are parallel to the incident ion beam direction, indicating that geometric shadowing [64] significantly contributes to shaping the dots. But, in contrast with the continuum models of shadowing in thin film growth [63], our valley areas are rarely shadowed from the incident ion beam, and they still efficiently work as loci for the IBI morphological instability inducing dot formation. After  $t_c$ , however, most of the valley regions of the cells are shadowed, and the shadowing effects do play a significant role in the evolution of the cellular pattern under our experimental irradiation conditions; figure not shown.

## 2. Cellular pattern

For the formation of the cellular pattern, the wall interconnection needs to be operative, in addition to the sputtering and mass displacement responsible for the formation of the dot pattern, making the scaling behavior of the cellular structures at  $t > t_c$  different from that displayed by the dots at  $t < t_c$ . Recall that for long irradiation times, the surface slope distribution becomes distinctively  $t$  independent [Fig. 6(c)]. This fact, combined with the coarsening process, makes this pattern statistically self-similar, see Fig. 14. Specifically, in this figure a small part of an AFM snapshot taken at  $t = 450$  min  $> t_c$  [panel (a)] is rescaled [panel (b)] to have the same correlation length  $\xi(t)$  as an AFM image taken at a larger  $t$  with the same size of the original image [panel (c)]. The disordered surfaces of panels (b) and (c) have the same statistical properties, which implies self-similarity (in statistical terms)

for the underlying space-time process. This type of behavior is frequent in many evolving natural and artificial cellular structures, having also been reported for, e.g., thin films grown by chemical vapor deposition displaying cauliflowerlike morphologies [21] or for Si surfaces ion-etched by magnetron sputtering [65].

*Rescattering.* During plasma etching where a solid surface is etched by an incident reactive ion beam such as  $\text{SF}_6$ , foamlike cellular structures develop. To elucidate the ensuing pattern formation, Drotar *et al.* [66] proposed that a substantial amount of the incident ions rescatter from their initial landing positions and further etch the surface, in particular, near surface depressions, seriously destabilizing the morphology. Kinetic Monte Carlo simulations of a discrete model which implements etching by rescattered ions reproduces these experimental observations, in particular, the scaling behavior with critical exponents  $\alpha = \beta = z = 1$ .

The exponent values predicted by the discrete model [66] are similar to our experimental observations for  $t < t_c$ , while the cellular morphologies seen in Ref. [66] resemble those we observe for  $t > t_c$ . However, no change in the basic pattern motif with time is found in the reactive ion etching experiment or model [66]. We examine whether the rescattering model is applicable in our experimental conditions, where high-energy, chemically inactive ions are employed in contrast to the low energy, reactive ions employed in Ref. [66].

We have performed SRIM simulations with 2 keV  $\text{Ar}^+$  or  $\text{Kr}^+$  ions for incident angle  $\theta = 78^\circ$ . We choose this value of  $\theta$ , instead of  $72^\circ$  as in our experiments, because the slope of the surface structures, estimated from  $\arctan(W/\lambda)$  is around  $6^\circ$ , so the *local* incidence angle with respect to the surface normal becomes  $78^\circ$ . These simulations find that only 4.5% and 7%, respectively, of the incident ions rescatter to the

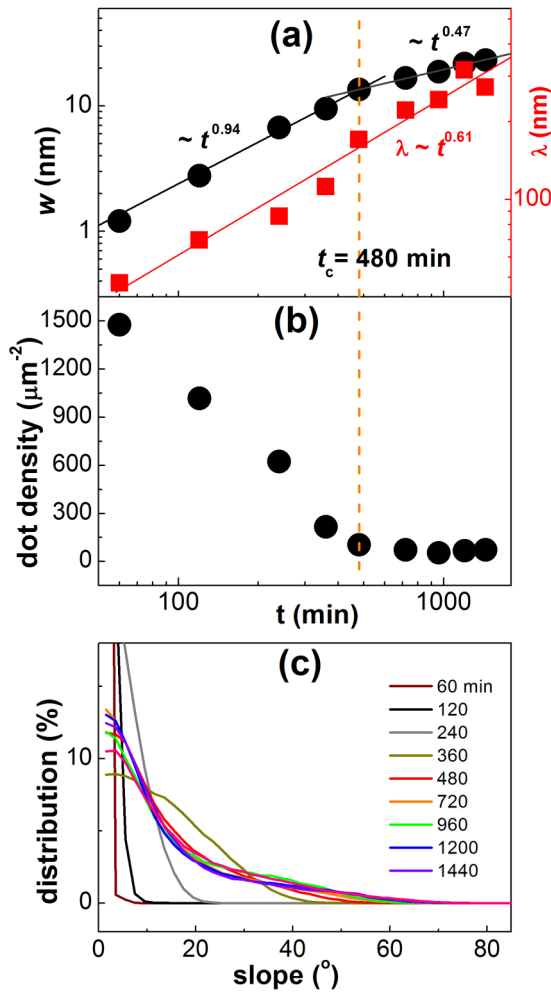


FIG. 16. Fluence dependence of (a) the surface roughness  $W(t)$  (left vertical axis) and dot wavelength (right vertical axis), (b) the areal dot density  $\sigma(t)$ , and (c) the local slope distribution for  $\text{Ar}^+$  irradiation of rotating targets. The dashed vertical line in (a) and (b) is at  $t = 480$  min. The solid black lines in (a) and (b) represent power-law behavior as  $W(t) \sim t^\beta$  for the values of  $\beta$  indicated in each case, and the solid red lines represent power-law behavior as  $\lambda(t) \sim t^n$  for the value of  $n$  which is given.

neighboring surface in contrast to a rescattering probability close to 1 during plasma etching [66]. In addition, the mean energy of the rescattered ions decreases substantially, close to 250 eV, which implies a reduced sputter yield, while the reduced energy of the rescattered reactive ions increases the etching efficiency by increasing the dwell time near the surface. Thus, ion rescattering should play a minor role in the surface dynamics under our present experimental conditions.

**Cellular structures.** A submicron cellular surface structure made up of cells which coarsen with time has been experimentally reported for ion plasma etching of silicon targets [20,21,65] with a strong resemblance to the cellular pattern observed in our experiments for  $t > t_c$ . The surface dynamics has been quantitatively described [65] by a continuum model which is a certain generalization of the Cahn-Hilliard equation [26]. Once more, no change in the basic pattern motif with time was found, in contrast with our present experiments,

but the cellular structure does reach a dynamical regime in which the coarsening exponent is approximately 0.5 [65], close to the one we measure. Interestingly, such a coarsening (so-called parabolic) law was proven by Mullins in the context of grain growth under the hypothesis of statistical self-similarity for the surface, combined by a scaling condition for the local grain velocity [67].

## VI. SUMMARY AND CONCLUSIONS

We have employed a 2 keV  $\text{Kr}^+$  ion beam to irradiate azimuthally rotating HOPG(0001) targets, whose behavior under such Zalar rotation protocol happens to differ from what had been previously found, e.g., on semiconductor targets like Si. In our experiments, a disordered surface pattern forms, whose basic motif is found to evolve from a dot to a cellular structure as the ion fluence increases. The cellular structure develops from the concatenation of previous dots, which later transform into continuous walls. These walls form a global network, converting the individual cells into a full-fledged cellular pattern. Such a change in the elemental pattern motif has never been reported for analogous systems, to the best of our knowledge.

We can elucidate the pattern evolution from that seen on stationary HOPG(0001) targets under the same irradiation conditions. For these, the stack of graphene layers is preferentially exposed to the ion beam at grain boundaries. There, the dots grow faster and become concatenated to form walls along the illuminated side of the grain boundaries. When the substrate is rotated during irradiation, the walls develop around the grain boundaries and form a global network of walls. This picture is consistent with the observation of the same growth and coarsening exponent values characterizing the surface patterns on both the rotating and the stationary substrates. Furthermore, a very similar change in the pattern motif and scaling behavior are also observed for patterns produced on rotating HOPG by IBI with  $\text{Ar}^+$  ions under otherwise the same irradiation conditions, as detailed in the Appendix, while the cellular pattern had also been reported to form under slightly higher incidence angle conditions [22]. The common observation of the unique pattern evolution which we are reporting supports the robust role of the higher exposure to irradiation at grain boundaries. From a general point of view, our present paper also underscores the need to take into consideration grain boundaries for a complete understanding of nanopattern formation on polycrystalline surfaces.

We have examined whether the observed pattern evolution can be reproduced by continuum models for nanopattern formation via IBI of rotating targets. Previous height equations predict close-packed patterns characterized by a single length scale [14–16]. With the aim to overcome this limitation, we have considered a recent continuum nonlinear model based on viscous relaxation of ion-induced stress [24]. The model is able to reproduce some of our experimental observations in the dot pattern regime. However, our simulations have not reached the cellular pattern seen in experiments for large fluences. We believe this is largely due to the lack of two important ingredients in the current continuum model, namely, noise and a proper account of the way in which the substrate grain structure alters the irradiation process. As discussed in

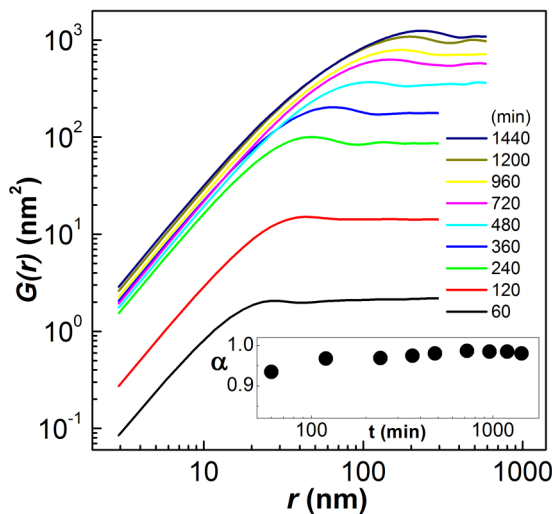


FIG. 17.  $G(r, t)$  as a function of distance for fluence values as in the legend, for IBI of rotating HOPG(0001) targets using  $\text{Ar}^+$  ions. The inset shows the value of the roughness exponent  $\alpha$  as a function of  $t$ .

previous sections, many of the quantitative and qualitative shortcomings of the model could possibly be circumvented if progress is made along those two avenues, constituting computational challenges in both cases. Additional improvements may also come from the consideration of nonlocal effects, such as geometric shadowing and the roles of bubbles formed by incorporation of the incident ions [68].

We finally note that hole or cellular patterns which are analogous to the ones we are presently reporting on, can form by IBI of *stationary* substrates, provided the diffusivity of adatoms is so high that they efficiently adhere to the edges of pre-existing structures, so vacancies become the rate-limiting ad-species. Such a high adatom diffusivity is achieved at elevated substrate temperatures. For instance, Ou *et al.* [69,70] and Engler *et al.* [71] produced nanohole patterns on *stationary* Ge and Si surfaces at such high substrate temperatures that the substrates remain crystalline. Hole patterns have also been reported on stationary Si [72,73] and Ge [73] targets via IBI with concurrent impurity deposition. In contrast with all these various works, our present IBI experiments have been carried out on rotating HOPG(0001) targets, at room temperature, and without impurity co-deposition, clearly demonstrating the formation of the enclosure network by concatenated dots as a salient mechanism for the formation of a submicron cell pattern.

**ACKNOWLEDGMENTS**

This work was supported by the Korean Research Foundation through Grants No. NRF- 2016R1D1A1B03930532

and No. 2019R1F1A1040955, by Ministerio de Economía, Industria y Competitividad (MINECO, Spain), Agencia Estatal de Investigación (AEI, Spain), and Fondo Europeo de Desarrollo Regional (FEDER, EU) through Grants No. PGC2018-094763-B-I00, No. PID2019-106339GB-I00, and No. PID2019-109320GB-I00, and by Comunidad de Madrid (Spain) under the Multiannual Agreement with UC3M in the line of Excellence of University Professors, No. EPUC3M23, in the context of the V Plan Regional de Investigación Científica e Innovación Tecnológica (PRICIT).

**APPENDIX: EXPERIMENTAL RESULTS USING  $\text{Ar}^+$  IONS**

This Appendix collects results obtained for IBI of rotating HOPG(0001) targets using  $\text{Ar}^+$  ions, under otherwise the same irradiation conditions (ion energy, incidence angle, and target rotation speed) as employed in the main text for the case of  $\text{Kr}^+$  ions.

Figure 15 shows the fluence dependence of the surface morphologies and is the analog of Fig. 2 of the main text. An isotropic disordered dot pattern forms for relatively small fluences  $t < t_c$ . These dots coarsen with increasing fluence and evolve into a cellular pattern for larger fluences  $t > t_c$  which coarsens for as long as the experiments proceed. The characteristic fluence value which separates the dot and cellular structure now is estimated as  $t_c \approx 460$  min ( $F = 4432$  ions/ $\text{nm}^2$ ) from the behavior of the surface roughness shown in Fig. 16. Similarly to the  $\text{Kr}^+$  ion case, the roughness increases as a power law with  $t$  as  $W(t) \sim t^\beta$ , with exponent values  $\beta_1 \approx 0.94$  ( $\beta_2 \approx 0.47$ ) for  $t < t_c \approx 480$  min ( $t > t_c$ ), very close to those discussed in the main text. Qualitatively, the dot density has a very similar behavior as that seen in Fig. 6(b) and the slope distribution also behaves as in the  $\text{Kr}^+$  case, most notably becoming largely  $t$  independent for  $t > t_c$ . As in Fig. 8, the coarsening exponent value is the same in the low and high fluence regimes and has a value  $n = 0.61$  which is quite close to that obtained for  $\text{Kr}^+$  ions.

Finally, Fig. 17 shows the height-difference correlation function  $G(r, t)$  as a function of distance for different  $t$  values. Now, similar to Fig. 7(a), there is power-law scaling as  $G(r, t) \sim r^{2\alpha}$  for  $r < \xi(t)$  and saturation to an  $t$ -dependent value for  $r > \xi(t)$ , with  $\xi(t)$  an  $t$ -increasing length scale which is quantitatively close to the average size of the main motif of the pattern (dot for  $t < t_c$  and cellular structure for  $t > t_c$ ) for  $\alpha \approx 1$  values of the roughness exponent, as in the  $\text{Kr}^+$  ion case. Overall, all the behaviors found for  $\text{Ar}^+$  ions coincide qualitatively with those discussed in the main text for  $\text{Kr}^+$  ions and also quantitatively from the point of view of scaling exponents.

[1] M. A. Nastasi, J. W. Mayer, and J. K. Hirvonen, *Ion-Solid Interactions: Fundamentals and Applications* (Cambridge University Press, New York, 1996).  
 [2] W. L. Chan and E. Chason, *J. Appl. Phys.* **101**, 121301 (2007).

[3] J. Muñoz-García, L. Vázquez, R. Cuerno, J. A. Sánchez-García, M. Castro, and R. Gago, in *Toward Functional Nanomaterials*, edited by Z. M. Wang (Springer, Dordrecht, 2009), pp. 323–398.

- [4] J. Muñoz-García, L. Vázquez, M. Castro, R. Gago, A. Redondo-Cubero, A. Moreno-Barrado, and R. Cuerno, *Mater. Sci. Eng.*, **R 86**, 1 (2014).
- [5] S. A. Norris and M. J. Aziz, *Appl. Phys. Rev.* **6**, 011311 (2019).
- [6] R. Cuerno and J.-S. Kim, *J. Appl. Phys.* **128**, 180902 (2020).
- [7] A. Zalar, *Thin Solid Films* **124**, 223 (1985).
- [8] E.-H. Cirlin, J. J. Vajo, R. E. Doty, and T. C. Hasenberg, *J. Vac. Sci. Technol. A* **9**, 1395 (1991).
- [9] F. Frost, A. Schindler, and F. Bigl, *Phys. Rev. Lett.* **85**, 4116 (2000).
- [10] F. Frost, B. Ziberi, T. Höche, and B. Rauschenbach, *Nucl. Instrum. Methods Phys. Res., Sec. B* **216**, 9 (2004).
- [11] F. Frost, B. Ziberi, A. Schindler, and B. Rauschenbach, *Appl. Phys. A* **91**, 551 (2008).
- [12] D. Chowdhury, D. Ghose, and B. Satpati, *Mater. Sci. Eng.: B* **179**, 1 (2014).
- [13] T. Basu, D. A. Pearson, R. M. Bradley, and T. Som, *Appl. Surf. Sci.* **379**, 480 (2016).
- [14] R. M. Bradley and E.-H. Cirlin, *Appl. Phys. Lett.* **68**, 3722 (1996).
- [15] R. M. Bradley, *Phys. Rev. E* **54**, 6149 (1996).
- [16] J. Muñoz-García, R. Cuerno, and M. Castro, *J. Phys.: Condens. Matter* **21**, 224020 (2009).
- [17] T. Yasserli and R. Kree, *Nucl. Instrum. Methods Phys. Res., Sect. B* **268**, 2496 (2010).
- [18] P. Sigmund, *Phys. Rev.* **184**, 383 (1969).
- [19] Z. Yang, M. A. Lively, and J. P. Allain, *Phys. Rev. B* **91**, 075427 (2015).
- [20] M. Castro, J. Muñoz-García, R. Cuerno, M. García-Hernández, and L. Vázquez, *New J. Phys.* **9**, 102 (2007).
- [21] M. Castro, R. Cuerno, M. Nicoli, L. Vázquez, and J. G. Buijnsters, *New J. Phys.* **14**, 103039 (2012).
- [22] S. M. Yoon and J. S. Kim, *J. Appl. Phys.* **119**, 205301 (2016).
- [23] A. Moreno-Barrado, R. Gago, A. Redondo-Cubero, L. Vázquez, J. Muñoz-García, R. Cuerno, K. Lorenz, and M. Castro, *Europhys. Lett.* **109**, 48003 (2015).
- [24] J. Muñoz-García, R. Cuerno, and M. Castro, *Phys. Rev. B* **100**, 205421 (2019).
- [25] S. M. Yoon, J.-S. Kim, D. Yoon, H. Cheong, Y. Kim, and H. H. Lee, *J. Appl. Phys.* **116**, 024307 (2014).
- [26] R. C. Desai and R. Kapral, *Dynamics of Self-organized and Self-assembled Structures* (Cambridge University Press, Cambridge, UK, 2009).
- [27] A. L. Mackay and H. Terrones, *Nature (London)* **352**, 762 (1991).
- [28] T. Lenosky, X. Gonze, M. Teter, and V. Elser, *Nature (London)* **355**, 333 (1992).
- [29] K. Takahiro, K. Zhang, F. Rotter, D. Schwen, C. Ronning, H. Hofsäss, and J. Krauser, *Nucl. Instrum. Methods Phys. Res., Sec. B* **256**, 378 (2007).
- [30] K. Takahiro, K. Ozaki, K. Kawatsura, S. Nagata, S. Yamamoto, K. Narumi, and H. Naramoto, *Appl. Surf. Sci.* **256**, 972 (2009).
- [31] M. Cross and H. Greenside, *Pattern Formation and Dynamics in Nonequilibrium Systems* (Cambridge University Press, Cambridge, England, 2009).
- [32] Y. Zhao, G.-C. Wang, and T.-M. Lu, *Characterization of Amorphous and Crystalline Rough Surface: Principles and Applications* (Academic Press, San Diego, CA, 2001).
- [33] A.-L. Barabási and H. E. Stanley, *Fractal Concepts in Surface Growth* (Cambridge University Press, Cambridge, England, 1995).
- [34] P. Sana, L. Vázquez, R. Cuerno, and S. Sarkar, *J. Phys. D: Appl. Phys.* **50**, 435306 (2017).
- [35] J. M. Lopez, M. A. Rodríguez, and R. Cuerno, *Physica A* **246**, 329 (1997).
- [36] T. J. Oliveira and F. D. A. Aarão Reis, *J. Appl. Phys.* **101**, 063507 (2007).
- [37] T. J. Oliveira and F. D. A. Aarão Reis, *Phys. Rev. E* **83**, 041608 (2011).
- [38] E. Vivo, M. Nicoli, M. Engler, T. Michely, L. Vázquez, and R. Cuerno, *Phys. Rev. B* **86**, 245427 (2012).
- [39] M. Siegert, *Phys. Rev. E* **53**, 3209 (1996).
- [40] R. M. Bradley and J. M. E. Harper, *J. Vac. Sci. Technol. A* **6**, 2390 (1988).
- [41] G. Carter and V. Vishnyakov, *Phys. Rev. B* **54**, 17647 (1996).
- [42] M. Castro, R. Cuerno, L. Vázquez, and R. Gago, *Phys. Rev. Lett.* **94**, 016102 (2005).
- [43] J. Muñoz-García, M. Castro, and R. Cuerno, *Phys. Rev. Lett.* **96**, 086101 (2006).
- [44] R. Cuerno and A.-L. Barabási, *Phys. Rev. Lett.* **74**, 4746 (1995).
- [45] J. Muñoz-García, R. Gago, L. Vázquez, J. A. Sánchez-García, and R. Cuerno, *Phys. Rev. Lett.* **104**, 026101 (2010).
- [46] A. Moreno-Barrado, M. Castro, R. Gago, L. Vázquez, J. Muñoz-García, A. Redondo-Cubero, B. Galiana, C. Ballesteros, and R. Cuerno, *Phys. Rev. B* **91**, 155303 (2015).
- [47] A. Oron, S. H. Davis, and S. G. Bankoff, *Rev. Mod. Phys.* **69**, 931 (1997).
- [48] R. V. Craster and O. K. Matar, *Rev. Mod. Phys.* **81**, 1131 (2009).
- [49] S. E. Orchard, *Appl. Sci. Res. A* **11**, 451 (1963).
- [50] W. W. Mullins, *J. Appl. Phys.* **28**, 333 (1957).
- [51] W. W. Mullins, *J. Appl. Phys.* **30**, 77 (1959).
- [52] J. Muñoz-García, R. Gago, R. Cuerno, J. Sánchez-García, A. Redondo-Cubero, M. Castro, and L. Vázquez, *J. Phys.: Condens. Matter* **24**, 375302 (2012).
- [53] J.-H. Kim, J.-S. Kim, J. Muñoz-García, and R. Cuerno, *Phys. Rev. B* **87**, 085438 (2013).
- [54] S. Kumar Garg, R. Cuerno, D. Kanjilal, and T. Som, *J. Appl. Phys.* **119**, 225301 (2016).
- [55] A. Moreno-Barrado, M. Castro, J. Muñoz-García, and R. Cuerno, *Nucl. Instrum. Methods Phys. Res., Sec. B* **365**, 13 (2015).
- [56] C. S. Madi, E. Anzenberg, K. F. Ludwig, Jr., and M. J. Aziz, *Phys. Rev. Lett.* **106**, 066101 (2011).
- [57] S. Nestic, R. Cuerno, E. Moro, and L. Kondic, *Eur. Phys. J.: Spec. Top.* **224**, 379 (2015).
- [58] S. Nestic, R. Cuerno, E. Moro, and L. Kondic, *Phys. Rev. E* **92**, 061002(R) (2015).
- [59] Y. Zhang, J. Sprittles, and D. Lockerby, *J. Fluid Mech.* **915**, A135 (2021).
- [60] S. Habenicht, W. Bolse, K. P. Lieb, K. Reimann, and U. Geyer, *Phys. Rev. B* **60**, R2200 (1999).
- [61] S. Habenicht, K. Lieb, W. Bolse, U. Geyer, F. Roccaforte, and C. Ronning, *Nucl. Instrum. Methods Phys. Res., Sec. B* **161-163**, 958 (2000).
- [62] S. Habenicht and K. P. Lieb, *AIP Conf. Proc.* **576**, 951 (2001).
- [63] J. H. Yao and H. Guo, *Phys. Rev. E* **47**, 1007 (1993).

- [64] G. Carter, *J. Appl. Phys.* **85**, 455 (1999).
- [65] M. Castro, R. Cuerno, M. M. García-Hernández, and L. Vázquez, *Phys. Rev. Lett.* **112**, 094103 (2014).
- [66] J. T. Drotar, Y.-P. Zhao, T.-M. Lu, and G.-C. Wang, *Phys. Rev. B* **61**, 3012 (2000).
- [67] W. W. Mullins, *Scr. Metall.* **22**, 1441 (1988).
- [68] H. Hofsäss and O. Bobes, *Appl. Phys. Rev.* **6**, 021307 (2019).
- [69] X. Ou, A. Keller, M. Helm, J. Fassbender, and S. Facsko, *Phys. Rev. Lett.* **111**, 016101 (2013).
- [70] X. Ou, K. H. Heinig, R. Hübner, J. Grenzer, X. Wang, M. Helm, J. Fassbender, and S. Facsko, *Nanoscale* **7**, 18928 (2015).
- [71] M. Engler and T. Michely, *Phys. Rev. B* **93**, 085423 (2016).
- [72] J. A. Sánchez-García, R. Gago, R. Caillard, A. Redondo-Cubero, J. A. Martín-Gago, F. J. Palomares, M. Fernández, and L. Vázquez, *J. Phys.: Condens. Matter* **21**, 224009 (2009).
- [73] Q. Wei, J. Lian, L. A. Boatner, L. M. Wang, and R. C. Ewing, *Phys. Rev. B* **80**, 085413 (2009).